

## **Anode-metal drop formation and detachment mechanisms in liquid metal batteries**

Benard, S.; Weber, N.; Horstmann, G. M.; Landgraf, S.; Weier, T.;

Originally published:

August 2021

**Journal of Power Sources 510(2021), 230339**

DOI: <https://doi.org/10.1016/j.jpowsour.2021.230339>

Perma-Link to Publication Repository of HZDR:

<https://www.hzdr.de/publications/Publ-31645>

Release of the secondary publication  
on the basis of the German Copyright Law § 38 Section 4.

CC BY-NC-ND

# Anode-metal drop formation and detachment mechanisms in liquid metal batteries

Sabrina Bénard<sup>a,b,\*</sup>, Norbert Weber<sup>a</sup>, Gerrit Maik Horstmann<sup>a</sup>, Steffen Landgraf<sup>a</sup>, Tom Weier<sup>a</sup>

<sup>a</sup>*Helmholtz-Zentrum Dresden – Rossendorf, Bautzner Landstr. 400, 01328 Dresden, Germany.*

<sup>b</sup>*Ecole Normale Supérieure Paris-Saclay, 4 avenue des Sciences, 91190, Gif-sur-Yvette, France.*

---

## Abstract

We study numerically localised short-circuits in Li||Bi liquid metal batteries. In the prototype of a classical, three liquid-layer system, we assume a perceptible local deformation of the Li-salt interface. We find that there exists always a critical current at which a Li-droplet is cut off from this hump, and transferred to the Bi-phase. In a second case, we assume that the molten Li is contained in a metal foam, and that a small Li-droplet emerges below this foam due to insufficient wetting. This droplet is deformed by Lorentz forces, until eventually being pinched off. Here, the critical current is slightly lower than in the three layer system, and both, a droplet transfer and complete short-circuits are observed. Finally, we discuss the relevance of our simulations for experimentally observed short-circuits and non-faradaic Li-transfer.

*Keywords:* liquid metal battery, OpenFOAM, volume-of-fluid method, contact angle, multiphase simulation, short-wave instability

---

## 1. Introduction

Liquid metal batteries have been proposed as cheap stationary energy storage about ten years ago [1]. Built by a stratification of two molten metal electrodes, separated by a fused salt electrolyte, such cells offer extreme current densities, self-healing properties and a potentially unlimited life-time. The ohmic resistance of the electrolyte layer

---

\*Corresponding author. Helmholtz-Zentrum Dresden – Rossendorf, Bautzner Landstr. 400, 01328 Dresden, Germany. *E-mail address:* s.benard@hzdr.de (S. Bénard)  
*Email address:* (Sabrina Bénard)

represents typically the highest overpotential of the cell [2–5]. Therefore, the electrolyte needs to be as thin as possible. Still, it should be thick enough to avoid any short-circuit between the metal electrodes. This optimisation problem leads to electrolyte layers, which are typically 5-10 mm thick. Paste electrolytes, where the molten salt is stabilised by a ceramic powder are usually only 1-3 mm thick [6–10], but exhibit a 2-4 times lower conductivity [5].

Apart from corrosion issues, internal short-circuits are one of the main reasons for cell failure, and have been reported e.g. for K-Hg [2, 6], Mg-Sb [11, 12], Li-Se [13, 14], Ca-Bi [15], and Li-BiPb cells [16]. As LMBs are mainly operated as closed cells, it has not always been easy to determine the reason for cell failure by post-mortem analysis. Especially in Ca-cells, dendrite-like intermetallic phases are known to grow into the electrolyte, finally short-circuiting the cell [15]. In Li||Sn batteries, Sn-rich particles have been observed inside the electrolyte [17]. Finally, it has been reported for Li-based cells that a low wettability of the current collector leads to droplet-shaped liquid electrodes, which decrease the interelectrode distance thus raising the risk for a short-circuit. Especially when using a metal foam as current collector – which should absorb the molten Li – a low wettability will lead to free-moving Li droplets, which may short-circuit the cell [14].

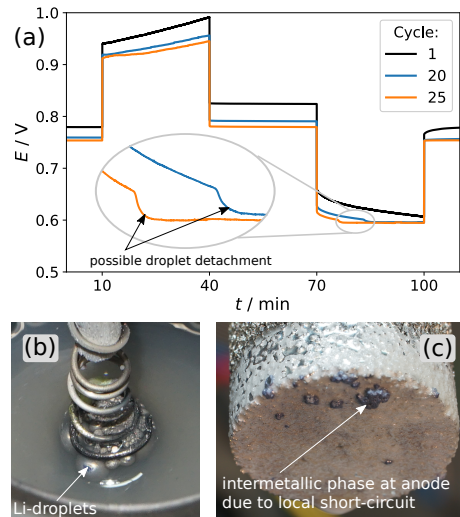


Figure 1: Charge-discharge curve of a Li||Bi liquid metal battery with sudden voltage drops (a), Li-droplets at the negative current collector (b) and intermetallic  $\text{Li}_3\text{Bi}$  formed at the current collector after local short-circuits (c).

Fig. 1 illustrates localised short-circuits observed in Li||Bi cells. The inset in the charge-discharge graph shows a sudden decrease in cell voltage – an effect, which happens especially after operating the cell for several cycles. We expect that such voltage-perturbations are caused by a short, non-faradaic transfer of Li from the anode to the cathode. Thus, the Li-concentration in the alloy will rise locally, therefore lowering the cell potential. Similar effects with a typically larger signature in the voltage profiles are known from vacuum arc-remelting [18] and electro-slag remelting [19], where the droplet transfer from the melting electrode to the pool is central to the refinement process.

One reason for the occurrence of sudden short-circuits might be an insufficient wetting of the current collector by liquid Li. This will lead inevitably to the formation of Li-droplets during charge, as illustrated in fig. 1b. If large enough, these droplets might be transferred to the positive electrode by, e.g., the Lorentz force or any fluid flow. A sufficient wetting is especially important when using a metal foam to contain the molten Li. Unexpected surface reactions, and missing wetting may lead to the formation of small Li-droplets below of the foam. The following inevitable short will

not only reduce the Coulombic efficiency, but might even lead to the formation of solid intermetallic  $\text{Li}_3\text{Bi}$ . In the worst case, the latter will attach to the metal foam – as illustrated in fig. 1c.

Inspired from aluminium-reduction cells, numerical modelling of liquid metal batteries has focused in the past mostly on very large single cells. Effects, which have been suspected to cause short-circuits include thermal convection [20–22], the Taylor instability [23–25], electro-vortex flow [26–30] as well as long-wave interface instabilities [31–42]. All these flow phenomena will rather cause long-wave, i.e. short-circuits of the complete battery. They are probably not suited to explain the experimental observations described before.

LMBs, which operate with three stratified layers, i.e. which do not use a metal foam to contain the anode metal, may suffer from localised short-circuits caused by short-wave interface instabilities. The latter have already been studied in relation to electric-arc furnaces by Sneyd [43]. He found that local currents can be destabilising if sufficiently strong. This work has later been revisited by Priede [44] in relation to LMBs. He found that the electromagnetic force has a stabilising effect on short-wave interface deformations, and that the latter are only unstable, if the electrolyte has a higher conductivity than the electrodes. However, this would be an atypical case. Of the more common electrode materials, only Se has a sufficiently low conductivity. For very strong, and non-linear interface deformations, also the kink- and pinch-type instability of liquid columns might be of interest [45].

The idea of a small Li-droplet, which forms due to insufficient wetting below of the metal-foam current collector resembles much the mercury electrode used for electrochemical investigations [46]. As long as the droplet is still in contact with the current collector, its surface will have a uniform potential. However, as soon as the drop detaches, this is not longer the case. As surface tension varies with the non-uniform potential, electrocapillarity will possibly change the shape of the droplet and drive Marangoni convection around it [46–48]. Electrocapillary motion might therefore explain the movement of droplets, but not its detachment.

A technical process, where droplet separation plays a crucial role, is classical arc welding. There, the shape, size and detachment of the fused metal droplets formed at

the tip of the electrode depends especially on the working current, i.e. the magnetic pinch force, and the welding gas, which determines surface tension [49–51]. The – very important – transition from globular transfer (of large) to spray transfer (of small droplets) has originally been explained by the static force balance theory (SFBT). The latter predicts a drop detachment if the retaining forces (surface tension) are larger than the separating forces (gravity, Lorentz force) [52–54]. Alternatively, the pinch instability theory (PIT) is used to explain droplet detachment [54]. There, a fluid column is expected to disintegrate into a droplet chain due to the destabilising effect of the welding current [49]. The observation of pinch effects on current bearing liquid columns dates back to Hering [55] and Northrup [56]. Alpher [57] gives an overview of the older contributions.

Droplet formation at and detachment from electrodes is vital to two metallurgical processes, namely vacuum arc remelting (VAR) and electroslag remelting (ESR). Both processes are used for the purification of metals that are melted by the passage of a large current. Drops of molten metal detach from the electrode and pass either through a vacuum (VAR) or through a slag layer (ESR) before entering a melt pool that eventually undergoes solidification. Typical current densities are  $50 \text{ kA/m}^2$  to  $100 \text{ kA/m}^2$  for ESR [58] and between  $1.5 \text{ kA/m}^2$  to  $600 \text{ kA/m}^2$  for VAR [59]. In both processes the detaching drops leave a very distinct voltage signature that is known as “voltage or resistance swing” in ESR [60]. Drop formation depends on the shape of the electrode (from completely flat to very spiky) which in turn is determined by the heat transfer conditions at the electrode [61]. Since the total current is usually high, vigorous electro-vortex flows are to be expected in these devices. They are strongest in the slag in case of ESR but – naturally – limited to the ingot for VAR [19]. In both processes droplets of high density material form at a downward facing interface in a low density environment, i.e. gravity can reasonably be expected to be the main cause of drop detachment and surface tension acts as a restoring force.

This is in sharp contrast to the situation in liquid metal batteries considered here: the droplets consisting of anode material possess a density lower than that of their environment. Thus, surface tension as well as gravity tend to keep the droplets at the anode. Obviously, the force balance needs to be extended in order to provide an expla-

nation for droplet detachment. For this purpose we will concentrate in the following on electromagnetic forces that were sometimes neglected [19, 61] but recently gained more attention [58, 62] in the frame of ESR models as well.

## 2. Model and numerics

We will present in this chapter the general model used for the studies, including geometry, material properties and the governing equations of the system. It will be applied in the next section to a Li|LiCl-LiF(70:30)|Bi liquid metal battery.

### 2.1. Geometry

The prototype used for the simulations is a cylinder. The diameter of this cylinder is  $D = 10$  cm, and the height of the three layers are  $H_p = 4.5$  cm,  $H_e = 1$  cm and  $H_n = 4.5$  cm for the positive electrode, the electrolyte and the negative electrode, respectively (figure 2). Generally, the negative electrode can consist of a liquid metal layer, floating on top of the electrolyte, or the molten Li may be contained in a metal foam. In order to study different droplet-transfer mechanism, we will include both set-ups in our model, denoting them as “foam” and “three-layer” case.

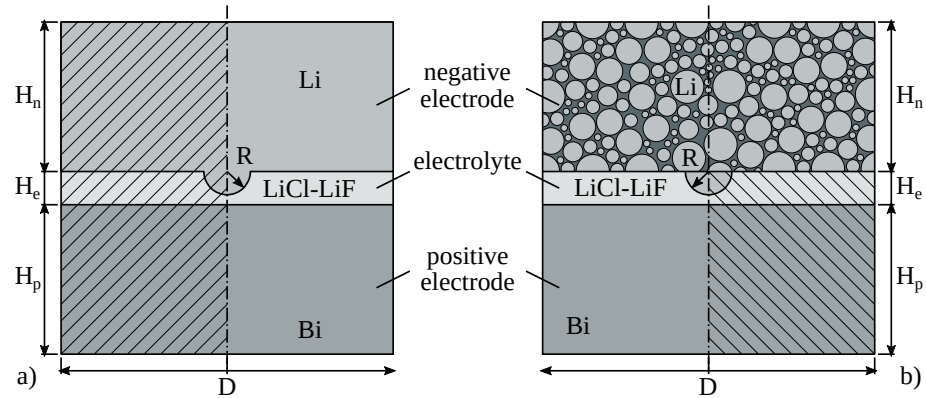


Figure 2: Sketch of the three-layer cell (a) and the cell featuring a foam containing the positive electrode material (b). The interface deformation/hemispherical droplet is located at the axis of symmetry. Numerical calculations are limited to the hatched regions.

The current collectors located above and below the battery will not be modelled, but will be replaced by simplified boundary conditions. The model will be set-up as being fully axisymmetric.

## 2.2. Material properties

We assume a typical working temperature of 550 °C for the Li|LiCl-LiF|Bi cell [63]. The following table gives an overview on the material properties.

Quantity	Unit	Li	salt	Bi
viscosity $\nu$	$\text{m}^2 \cdot \text{s}^{-1}$	$6.3 \cdot 10^{-7}$	$1.6 \cdot 10^{-6}$	$1.2 \cdot 10^{-7}$
density $\rho$	$\text{kg} \cdot \text{m}^{-3}$	482	1568	9721
electrical conductivity $\sigma$	$\text{S} \cdot \text{m}^{-1}$	$2.5 \cdot 10^6$	409	$6.9 \cdot 10^5$
reference		[64]	[65]	[66, 67]

The interface tension  $\gamma_{ij}$  between phases  $i$  and  $j$  is not known; we use therefore the following values, which have been estimated by Personnetaz et al. [22] for a similar system:

$$\gamma_{\text{Li,salt}} = 0.196 \text{N} \cdot \text{m}^{-1}, \quad (1a)$$

$$\gamma_{\text{Bi,salt}} = 0.275 \text{N} \cdot \text{m}^{-1}, \quad (1b)$$

$$\gamma_{\text{Li,Bi}} = 0.329 \text{N} \cdot \text{m}^{-1}. \quad (1c)$$

## 2.3. Equations

While computing the Lorentz force, the magnetic field originating from the feeding lines needs to be considered, as well. Simply neglecting the field generated by currents outside the fluids would lead to a reduced magnetic pressure towards the current collectors. The latter would drive a nonphysical fluid flow. In order to avoid the costly computation of additional magnetic fields, we employ the perturbed current method [33]. We approximate the battery's magnetic field as originating from an infinitely long cylinder, denoted as  $\mathbf{B}_0$ . This allows to compute simply the perturbed magnetic field  $\mathbf{b}$ . The total magnetic field in the battery will thus be  $\mathbf{B} = \mathbf{B}_0 + \mathbf{b}$ , and the current

density is written as  $\mathbf{J} = \mathbf{J}_0 + \mathbf{j}$  with  $\mathbf{J}_0 = -J_0\mathbf{e}_z$ . In order to find  $\mathbf{B}_0$ , we use Ampere's law

$$\oint \mathbf{B}_0 \cdot d\mathbf{l} = \iint \mu_0 \mathbf{J}_0 \cdot d\mathbf{S} \iff B_0(r) \cdot 2\pi r = \mu_0 J_0 \pi r^2,$$

with the vacuum permeability  $\mu_0$ . The magnetic field of the infinitely long cylinder reads then

$$\mathbf{B}_0(r) = \frac{\mu_0 J_0}{2} r \mathbf{e}_\theta. \quad (2)$$

The electric potential  $\varphi$  in the battery is obtained by solving the Laplace equation

$$\nabla \cdot (\sigma \nabla \varphi) = 0, \quad (3)$$

which is derived by applying the divergence operator to Ohm's law

$$\mathbf{J} = \sigma \mathbf{E} = \sigma(-\nabla \varphi + \mathbf{u} \times \mathbf{B}), \quad (4)$$

while neglecting the term  $\mathbf{u} \times \mathbf{B}$ . The latter is permissible, as the flow velocities are rather small. We find the current density as

$$\mathbf{J} = -\sigma \nabla \varphi. \quad (5)$$

The velocity  $\mathbf{u}$  is obtained by solving the Navier-Stokes equations

$$\frac{\partial(\rho \mathbf{u})}{\partial t} + \nabla \cdot (\rho \mathbf{u} \mathbf{u}) = -\nabla p_d + g z \nabla \rho + \nabla \cdot (\rho \nu (\nabla \mathbf{u} + (\nabla \mathbf{u})^T)) + \mathbf{J} \times \mathbf{B} + \mathbf{f}_{st}, \quad (6a)$$

$$\nabla \cdot \mathbf{u} = 0, \quad (6b)$$

with  $g$  denoting the gravity and  $p_d = p - \rho g z$  the modified pressure [68]. The surface tension force  $\mathbf{f}_{st}$  is modelled using the continuum surface force (CSF) model [69–72], i.e. it is implemented as a volume force  $\mathbf{f}_{st} = \sum_i \sum_{j \neq i} \gamma_{ij} \kappa_{ij} \delta_{ij}$ , concentrated at the interface, with  $\gamma_{ij}$  denoting the interface tension between phases  $i$  and  $j$ . The curvature is given as

$$\kappa_{ij} \approx -\nabla \cdot \frac{\alpha_j \nabla \alpha_i - \alpha_i \nabla \alpha_j}{|\alpha_j \nabla \alpha_i - \alpha_i \nabla \alpha_j|}, \quad (7)$$

and the Dirac delta function  $\delta_{ij} = \alpha_j \nabla \alpha_i - \alpha_i \nabla \alpha_j$  ensures that the force is applied only near an interface. Finally, we find the surface tension force as

$$\mathbf{f}_{st} \approx -\sum_i \sum_{j \neq i} \gamma_{ij} \nabla \cdot \left( \frac{\alpha_j \nabla \alpha_i - \alpha_i \nabla \alpha_j}{|\alpha_j \nabla \alpha_i - \alpha_i \nabla \alpha_j|} \right) (\alpha_j \nabla \alpha_i - \alpha_i \nabla \alpha_j). \quad (8)$$

Please refer to appendix Appendix A for further details about the surface tension and contact angle modelling.

We find the induction equation for the magnetic field  $\mathbf{b}$  by using Faraday's and Ohm's law

$$\nabla \times \delta \mathbf{e} = -\dot{\mathbf{b}}, \quad (9a)$$

$$\mathbf{j} = \sigma \delta \mathbf{e}, \quad (9b)$$

where  $\delta \mathbf{e}$  denotes the perturbed electrical field. Combining both equations leads to

$$\dot{\mathbf{b}} = -\nabla \times \delta \mathbf{e} = -\nabla \times \left( \frac{\mathbf{j}}{\sigma} \right) = -\nabla \left( \frac{1}{\sigma} \right) \times \mathbf{j} - \frac{1}{\sigma} \nabla \times \mathbf{j}. \quad (10)$$

Applying Ampere's law as

$$\nabla \times \mathbf{b} = \mu_0 \mathbf{j}, \quad (11)$$

we obtain

$$\nabla \times \mathbf{j} = \nabla \times \left( \frac{1}{\mu_0} \nabla \times \mathbf{b} \right) = \frac{1}{\mu_0} \left( \underbrace{\nabla(\nabla \cdot \mathbf{b})}_{=0} - \Delta \mathbf{b} \right) = -\frac{1}{\mu_0} \Delta \mathbf{b}. \quad (12)$$

Considering that the magnetic field varies slowly, i.e.  $\dot{\mathbf{b}} \approx \mathbf{0}$ , we can use the quasi-static approximation [25, 73, 74] and obtain the final induction equation as

$$\frac{1}{\mu_0} \Delta \mathbf{b} = \sigma \nabla \left( \frac{1}{\sigma} \right) \times \mathbf{j}. \quad (13)$$

Due to the symmetry of the model, the only non-zero component of the magnetic field is the azimuthal part  $b_\theta$ . Indeed, as the system is axisymmetrical, every meridional plane containing the vectors  $\mathbf{e}_z$  and  $\mathbf{e}_r$  is a symmetry plane for the current. Thus, the magnetic field is necessarily perpendicular to this plane, that is to say only in the azimuthal direction.

Knowing current and magnetic field, the Lorentz force is computed as

$$\mathbf{L}_f = \mathbf{j} \times \mathbf{B} + \mathbf{J}_0 \times \mathbf{b}. \quad (14)$$

Note that we do not include the constant part  $\mathbf{J}_0 \times \mathbf{B}_0$  as it is rotation-free and can therefore be included into the pressure gradient. As the magnetic field is purely azimuthal we find

$$L_{f,\theta} = J_z b_r - j_r b_z = 0. \quad (15)$$

Using a modified volume-of-fluid method [68, 75, 76], the phase fractions  $\alpha_i$  are solved as

$$\frac{\partial \alpha_i}{\partial t} + \nabla \cdot (\alpha_i \mathbf{u}) = 0, \quad (16)$$

using an approach similar to the Flux Corrected Transport method [77–81]. The mixture properties are then computed as

$$v = \frac{1}{\rho} \sum_i \alpha_i \rho_i v_i, \quad \sigma = \sum_i \alpha_i \sigma_i, \quad \rho = \sum_i \alpha_i \rho_i. \quad (17)$$

We implement our model in the open source CFD library OpenFOAM [82], using the existing solver *multiphaseInterFoam* [68, 76], where we add equation (3), (5), (13), as well as the Lorentz force in the equation (6a) [33].

#### 2.4. Boundary conditions

For every simulation, we use non-slip boundary conditions for the velocity as well as the corresponding Neumann boundary condition for pressure. Biot-Savart’s law might be applied to determine the correct boundary values of the magnetic field as [83, 84]

$$\mathbf{b}(\mathbf{r}) = \frac{\mu_0}{4\pi} \int \frac{\mathbf{j}(\mathbf{r}') \times (\mathbf{r} - \mathbf{r}')}{|\mathbf{r} - \mathbf{r}'|^3} dV'. \quad (18)$$

However, as the borders are far from the droplet, the perturbation of the magnetic field at the boundaries will be almost zero. We set therefore  $\mathbf{b} = \mathbf{0}$  on all boundaries, which saves much time by avoiding the computation of Biot-Savart’s law.

Finally, we fix the current density to  $-J_0 \mathbf{e}_z$  on the top and on the bottom of the battery, which is equivalent to fixing the gradient of the potential, since we have  $\nabla \varphi = -\frac{\mathbf{J}}{\sigma}$ .

#### 2.5. Contact angle

In order to model the Li-droplet in the foam case, we need to impose a contact angle between the droplet and the foam. It has been shown that the contact angle depends on several parameters such as the materials, the surface roughness and the temperature [85–87]. Moreover, the foam is a porous surface which means that the contact angle can take several values already because of its porosity [88]. Finally, the wetting properties

of the foam will also change during battery operation because of chemical reactions between salt and foam. Consequently, we do not know the exact value for the contact angle in our case. For this reason, we will limit the investigation to a  $90^\circ$  contact angle that approximate at the same time a mean value of the reported contact angles.

The shape of the droplet can be obtained by solving the Young-Laplace equation, which can be in our case re-written as

$$-\gamma \nabla \cdot \mathbf{n} = 2\gamma b + gz\Delta\rho, \quad (19)$$

where  $\mathbf{n}$  is the unit normal vector pointing out of the surface and  $b$  the curvature at the bottom of the drop.

An algorithm provided by Korhonen [89] allows us to compute the analytical solution of the shape of a droplet with desired material properties, contact angle and volume of the drop. We will use this algorithm in order to validate the solver.

### 3. Validation

The magnetohydrodynamic model has already been validated by comparison with an experiment [84]. Moreover, the multiphase model has been compared successfully with analytical results in the past [39, 84]. We will focus therefore on the validation of the contact angle, and the droplet shape.

For this purpose, we model a Li-droplet with a volume corresponding to the one of a half-sphere with a radius of 8 mm and a  $90^\circ$  contact angle. After placing this initial drop under the metal-foam, we run the simulation until the drop takes its final shape. Figure 3 shows this contour, while comparing it with the analytical solution obtained from Korhonen [89]. Overall, both curves match quite well. They deviate slightly only in the vicinity of the contours turning point. We denote the error  $\epsilon$  of the droplet shape as

$$\epsilon_r = \frac{h_a - h_n}{h_a}, \quad (20)$$

where  $h_a$  and  $h_n$  are the minimal height of the drop of the analytical and numerical solutions, respectively. We find  $\epsilon = 2.5\%$ , which we consider acceptable in terms of accuracy of our solver.

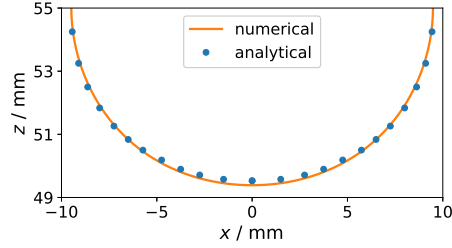


Figure 3: Shape of a Li-droplet on a surface obtained by the analytical solution (red) and numerics (black) for  $c_\alpha = 2$ ,  $\theta = 90^\circ$  and  $r = 8$  mm.

## 4. Results and discussion

### 4.1. Three liquid layers

As a first step, we study the three-layer case. A deformation of the Li-salt interface is used as initial perturbation. The latter is assumed to be of spherical shape in order to simplify the problem, and is placed at the centre of the battery so that we can use axisymmetrical simulations. Within the parameter studies, the radius and current density are varied.

Figure 4 illustrates the time evolution of the interface for a deformation with an initial radius of 8 mm. In the upper insets, a current density of  $4.4 \text{ A.cm}^{-2}$  has been applied. Here, the system re-stabilises by gravity: all Li floats up, until the deformation disappears. The same can be seen in the graph in the middle of the figure, which shows the minimal distance between the Li and Bi phases ( $d$ ) as a function of time. The blue curve, with a current density of  $4.4 \text{ A.cm}^{-2}$ , clearly confirms the re-stabilisation of the system: the inter-electrode distance increases with time until the interface regains its equilibrium shape.

The lower insets illustrate a second case with a larger current density of  $10 \text{ A.cm}^{-2}$ . Now, the resulting Lorentz force is large enough to destabilise the system. The Lorentz force acts predominantly at the upper right corner of the deformation as the current lines are strongly bent in this area. It overcomes the stabilising effect of surface tension, and shears off a Li-droplet within only  $\sim 15$  ms. This very quick pinch creates an inward directed flow, which might eventually push the droplet downwards to the Bi-phase.

This sequence of events is mirrored by the orange graph in fig. 4, which shows how the Li-droplet approaches the Bi-interface with time, until finally touching it. Please note that we do not observe a complete short-circuit, but just a droplet transfer from the negative to the positive electrode. Secondly, our axisymmetric model will probably not deliver a very realistic description of the droplets downwards-movement, because of its enforced axial-symmetry. The symmetry condition at the axis deflects the inward directed flow down- and upwards. In reality, this flow will probably be 3-dimensional. Nevertheless, we expect our model to describe the initial pinch- and cut-off-phase very well.

The discussion of figure 4 clearly indicates the existence of a critical current density, at which the system is destabilised, and a bubble pinched off from the negative electrode. In order to obtain the critical current, a parameter study with different deformation-radii and current has been performed. The results are presented in the table 1.

Droplet radius (mm)	Critical current density (A.cm <sup>-2</sup> )
3	14
4	11
5	8.4
6	6.6
7	5.5
8	4.7
9	4.1

Table 1: Critical current density depending on the radius of the initial deformation. The electrolyte is always 10 mm thick.

The table shows clearly that especially large deformations are prone to droplet formation and transfer. However, even there the current density is with 4 A/cm<sup>2</sup> still four times higher than for typical Li||Bi cells [90]. As quite violent flows will be required to create such large initial perturbations, we conclude that the appearance of short-wave instabilities is rather unlikely – at least for the Li||Bi system. This finding is perfectly

in line with Priede [44]. Finally, we would like to stress that even when a droplet cut-off appears, this does not necessarily lead to metal bridge between both electrodes. Typically, the Li-transfer occurs only in the form of droplets.

In order to transfer our results to other battery chemistries and geometries, it would be very useful to predict the critical cell currents by a simple analytical formula. Therefore, we seek to develop a first stability criterion in the following. The easiest way of estimating the resilience of the interface against perturbations is to compare the magnitude of the competing forces – as it is done for arc welding using the “static force balance theory” [52–54]. In general, both gravity and interfacial tension act as restoring forces, always counteracting displacements with respect to the equilibrium positions, i.e., perfectly flat interfaces possibly involving menisci in the vicinity of the contact lines. However, for predicting if spherical-like deformations will detach or not, interfacial tension is by far higher significance, because gravity, acting vertically, cannot compensate the horizontally concentrated Lorentz force, see figure 4. Hence, we assume that only the interfacial tension forces  $f_\gamma$ , for spherical perturbations of radius  $R$  simply scaling as

$$f_{\text{st}} \sim \gamma_{\text{Li,salt}} R, \quad (21)$$

compete against the Lorentz force. The delicate task is now to model the Lorentz force  $f_L$ , which is induced by the interface deformation itself. As the latter arises from the interaction of the cell current with its self-induced magnetic field, it will be of the order

$$f_L \sim \mu_0 I_p^2, \quad (22)$$

where  $I_p$  denotes the induced current contributing to the Lorentz force. The cell current  $I_0$ , which is purely vertical in unperturbed cells, only leads to a conservative Lorentz force distribution balanced by the pressure. Any interface displacement will lead to a redistribution of the cell current, which involves then a non-vertical component  $I_p$ , because the electrical resistance in the electrolyte is orders of magnitude higher than in the liquid metals. Hence, we need to calculate how strong  $I_0$  is deflected by given perturbations of the electrolyte – similar as described in [43, 91]. Assuming that the lower interface remains flat and  $\sigma_n, \sigma_p \gg \sigma_e$ , the horizontal perturbation current is of

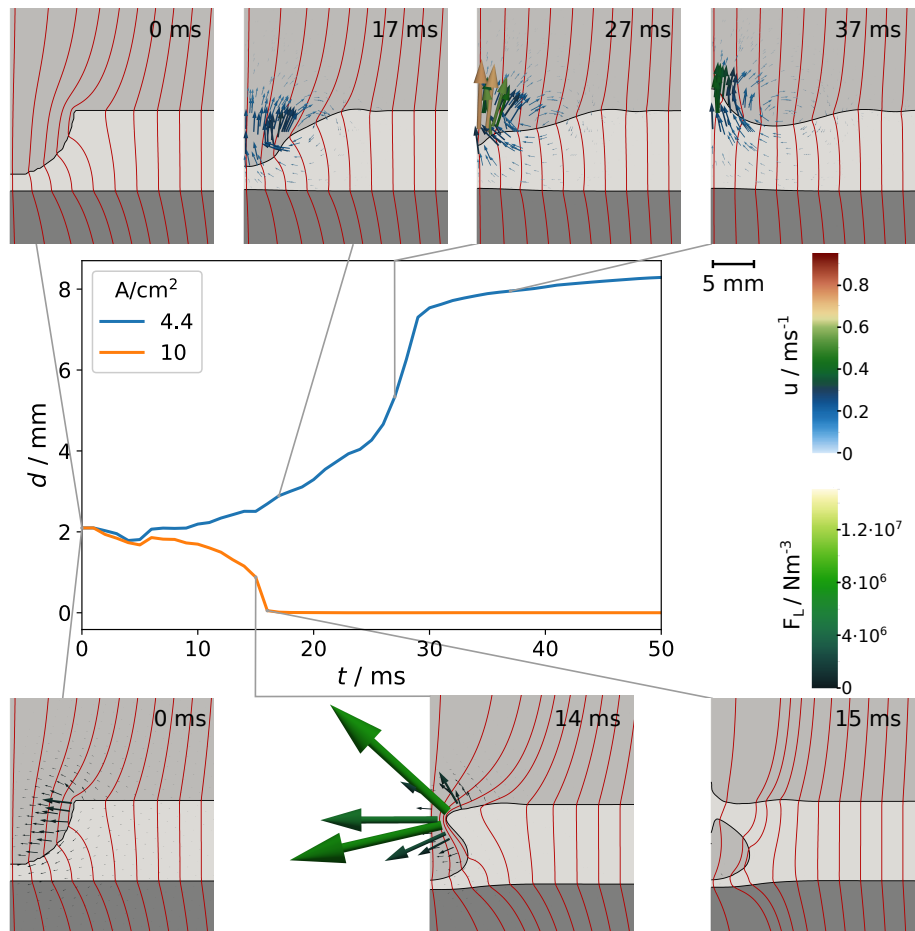


Figure 4: Minimal lithium-bismuth distance for the 3-layer simulation. The insets show the phases (grey), Lorentz force (green), current distribution (red) as well as the velocity (red/blue) for a case without (top) and with droplet-transfer (bottom).

the order

$$I_p \sim I_0 \frac{\eta}{H_e - \eta}, \quad (23)$$

where  $\eta$  is the characteristic depth of the perturbation. In the considered case of spherical droplets, we can identify  $\eta$  with the mean height of the half sphere  $\eta = 2R/3$ . Inserting (23) in (22) finally yields the scaling of the Lorentz force

$$f_L \sim \frac{\mu_0 I_0^2 R^2}{(3H_e - 2R)^2}. \quad (24)$$

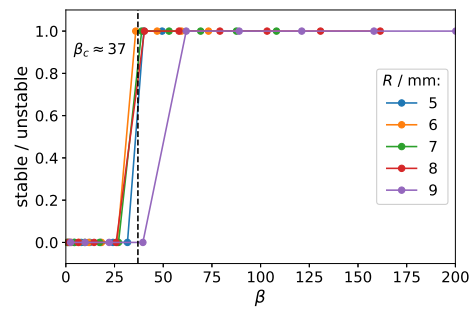
As the last step, we can construct a dimensionless parameter by comparing the forces  $f_L$  and  $f_{st}$  in the following way:

$$\beta := \frac{f_L}{f_{st}} = \frac{\mu_0 I_0^2}{\gamma_{Li,salt}} \frac{R}{(3H_e - 2R)^2}. \quad (25)$$

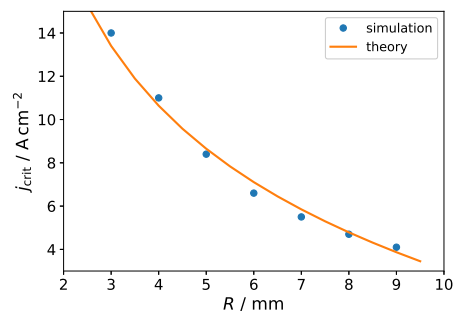
Lithium drops are expected to detach from the anode layer if  $\beta$  exceeds some critical threshold  $\beta > \beta_c$ . This statement is verified in figure 5 (a), showing the stability as a function of  $\beta$  for the different simulated drop radii shown in table 1. A sharp instability onset of  $\beta_c \approx 37$  becomes clearly apparent; only the largest  $R = 9$  mm sphere deviates significantly. The reason is most likely that gravity cannot be neglected anymore for such large  $R$  – here we reach the limits of the applied simplifications. However, all other cases give evidence that  $\beta$  predicts the interfacial stability adequately. Knowing  $\beta_c$ , we can rearrange equation (25) to further predict the critical cell currents

$$I_c = \sqrt{\frac{\beta_c \gamma_{Li,salt}}{\mu_0} \frac{(3H_e - 2R)}{\sqrt{R}}}, \quad (26)$$

above which the interface is unable to resist perturbations of size  $R$ . In figure 5 (b), we compare the simulated critical cell currents against equation (26). Again, a good agreement with respect to the uncertainties is evident, suggesting that the simplistic stability parameter (25) already reflects the essential physics. Up to here,  $\beta_c$  remains as an empirical parameter. It is expected to highly depend on the geometrical cell parameters, such as the cell diameter, and the material properties. A more rigorous analysis will be necessary for an analytical prediction of  $\beta_c$  – a promising task we leave open for future studies.



(a)



(b)

Figure 5: Critical parameter for instability (a) and critical parameter depending on current density (b). The current density is computed using the area of the full cell.

#### 4.2. Metal foam electrode

In this section we assume that the liquid Li, which forms the upper electrode, is contained in a metal foam. We focus on the idea that a small Li-droplet forms below of this foam due to insufficient wetting between foam and Li. We investigate, if this droplet will be transferred to the Bi-phase, or will keep its shape and position. The size of the droplet will be varied as well as the current density, exactly as in the previous section.

All simulations are performed in two steps: first, the setup is initialised with a hemispherical droplet of desired size and with a contact angle of  $90^\circ$ . Then, we run the solver without Lorentz force until the droplet takes its equilibrium shape. Finally, we launch the solver another time, but now with the Lorentz force, in order to observe a possible deformation or movement of the droplet.

As a first case, we use a Li-drop with an initial radius of  $R = 8$  mm. Figure 6 illustrates the minimal distance between Li and Bi over time. We see clearly that the drop oscillates, if the current density is below of  $J = 2.45 \text{ A.cm}^{-2}$ . While these oscillations are dampened for low currents, they lead to some kind of short-circuit for current densities between 2.45 and  $2.5 \text{ A.cm}^{-2}$ . At even higher current, no oscillation appears, and the inter-electrode distance drops quickly to zero – which indicates an immediate short-circuit, or a droplet cut-off and transfer to the Bi-electrode.

The insets in the same figure illustrate the droplet shape over time for  $J = 2.45 \text{ A.cm}^{-2}$ , i.e. the case with initial oscillation and final short-circuit. When switching the current on, the strong Lorentz force pinches the drop thus stretching it downwards. Surface tension and gravity, trying to counteract this movement, push the droplet again against the foam. These opposing forces, and the hysteresis between them, explain perfectly the oscillation, which finally leads to a short-circuit after only 0.272 s. Please note that the rather large drop leads rather to a direct contact of the Li- and Bi-phase than to droplet detachment and subsequent transport.

In a second case we study a smaller droplet with an radius of  $r = 6$  mm, as illustrated in figure 7. In this case, the critical current density is  $J = 3.5 \text{ A.cm}^{-2}$ , i.e. it is 40% higher than for the 8 mm droplet. Yet here, the insets shown for  $J = 3.5 \text{ A.cm}^{-2}$  indicate that neither an oscillation nor a short-circuit appear now. The droplet deforms,

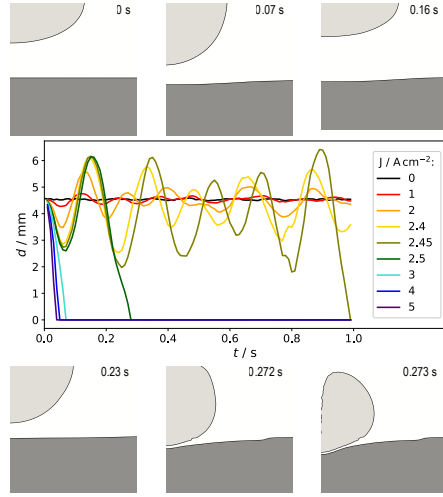


Figure 6: Minimal distance between lithium and bismuth for different current densities, and an initial droplet diameter of  $R = 8$  mm. The insets illustrate oscillation of the droplet with a final short-circuit for  $J = 2.45$  A/cm<sup>2</sup>. The electrolyte layer is 10 mm thick.

and simply detaches, before being transferred to the Bi-phase.

Table 2 summarises the different critical current densities for radii in the range [6 mm, 9 mm]. Exactly as in the three-layer case, smaller droplets need larger currents to detach. However, the critical current densities now lower than in the three-layer case, and thus more realistic. Furthermore, we observe short-circuit already at a droplet radius of  $r = 7$  mm – which was not the case in the tree-layer simulations.

Droplet radius (mm)	Critical current density (A.cm <sup>-2</sup> )
6	3.5
7	3
8	2.5
9	2.3

Table 2: Critical current for droplet detachment for the foam-case.

In order to investigate the nature of the droplet-oscillation further, we run the simu-

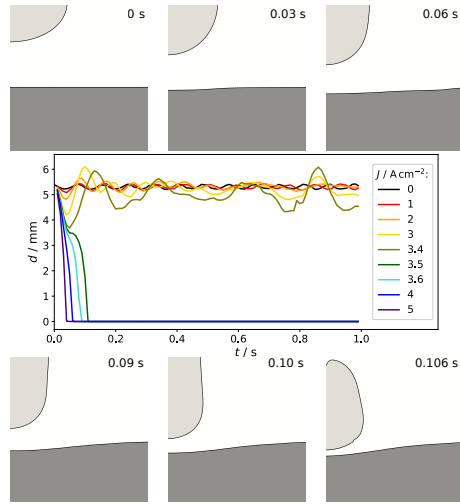
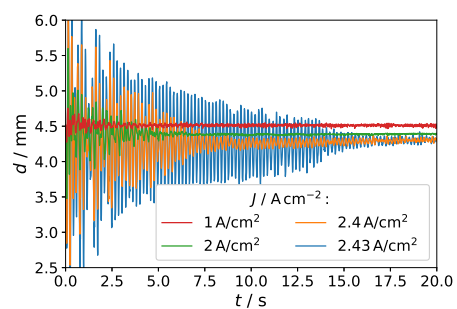


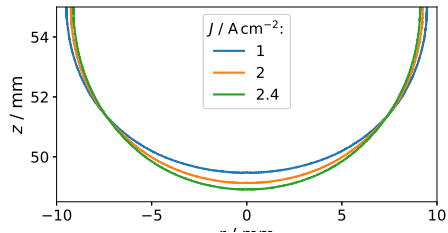
Figure 7: Minimal distance between lithium and bismuth for different current densities, and an initial droplet diameter of  $R = 6$  mm. The insets illustrate oscillation of the droplet with a final short-circuit for  $J = 3.5$  A/cm<sup>2</sup>. The electrolyte layer is 10 mm thick.

lation for  $r = 8$  mm until reaching a steady state. Figure 8a illustrates the time evolution of the interelectrode distance  $d$  for different current densities. As expected, the oscillation amplitude increases with current density, and becomes significantly high when approaching the critical current. In all cases, the oscillations are dampened with time until a steady state is reached. Interestingly, the final interelectrode distance depends on the current density, which means that the steady shape of the droplet depends on the cell current. These “final” shapes are represented for three current densities in figure 8b. We can clearly see that larger current pinches the droplet thus stretching it downwards. Apparently, the Lorentz force is not strong enough to detach the drop, but sufficiently strong to deform it – leading to a new balance between the forces.

Although we have shown that Lorentz forces can deform and even cut off Li-droplets, it is not easy to generalise our findings. The problem is simply too complex. While we used a 10 mm-thick electrolyte, it might be much thinner in other cases. While we assumed a contact angle between droplet and metal foam of  $90^\circ$ , the latter might approach  $180^\circ$  in certain cases – see fig. 1 for an example. Impurities, which attach to the interfaces, may alter the interface tension considerably. If the metal foam



(a)



(b)

Figure 8: Minimal distance between lithium and bismuth (a), and stationary droplet shape (b) for an initial droplet radius of 8 mm. The electrolyte layer is 10 mm thick.

is not filled with Li any more, the current needs to follow the metal mesh. This might lead to a very concentrated current entry into the droplet, and therefore even stronger Lorentz forces. Finally, the electrolyte layer will change its thickness during operation, and the droplet its volume. All these effects, or uncertainties, make it difficult to predict, when a droplet transfer from the negative to the positive electrode will happen. These uncertainties notwithstanding, the scenario sketched above plausibly explains the experimentally observed effects illustrated in fig. 1.

## 5. Summary

Focusing on Li||Bi liquid metal batteries (LMBs), we have investigated localised short-circuits, as well the transfer of Li-droplets from the negative to the positive electrode. After giving experimental evidence for such effects, we have studied two paradigmatic cases.

Firstly, we focused on a classical, three-layer LMB, where we imposed an initial deformation of the Li-salt interface. We find that there exists always a critical cell current, for which the resulting Lorentz force cuts off a Li-droplet. This drop is eventually transferred to the Bi-electrode. As the necessary current is fairly high, and the initial perturbation large, we conclude that such short-wave instabilities are rather unlikely to occur in reality. Moreover, we have shown that they do not lead to a localised short-circuit, but only to a droplet detachment and transfer.

Secondly, we considered an LMB, where the Li is contained in a current collector made of metal foam. Assuming that due to insufficient wetting small Li-droplets form below of this foam, we studied the influence of the cell current on this droplet. Here again, we found a critical current, which leads to droplet detachment caused by the pinching Lorentz force. At cell currents slightly below of the threshold, we observed a droplet-oscillation leading finally to a stable, stretched shape of the Li-drop. If the electrolyte is sufficiently thin, even a direct metal bridge from the negative to the positive electrode may appear. We believe that such effects offer a plausible explanation for the experimental observations described in the introduction.

An extension of this work would be the study of a larger range of contact angles

in order to understand its impact on the destabilisation, and of thicknesses of the electrolyte in order to find a minimal height of the electrolyte from which the destabilisation does not occur anymore.

## 6. Acknowledgement

This work was supported by a predoctoral scholarship of ENS Paris-Saclay, by the Deutsche Forschungsgemeinschaft (DFG, German Research Foundation) by award number 338560565 and in frame of the Helmholtz - RSF Joint Research Group “Magnetohydrodynamic instabilities: Crucial relevance for large scale liquid metal batteries and the sun-climate connection”, contract No. HRSF-0044 and RSF-18-41-06201. Fruitful discussions with W. Herreman and C. Nore are gratefully acknowledged.

## Appendix A. Nonphysical droplet oscillations

When validating the model, and simulating a single droplet, we often observed strong oscillations of the interface shape – even if we did not apply any Lorentz force. Such oscillations are clearly nonphysical, and have been observed by others, before [92, 93]. The reason for their appearance might be related to the poor interface curvature calculation of the CSF model, together with interFoam’s contact angle model [94–98].

The simplest remedy to suppress the oscillation is increasing the viscosity, as already reported by Guilizzoni [92, 93]. Further, a relaxation of the phase fraction or pressure, as well as a strong interface compression will help to damp the oscillation. However, the interface compression will deform the drop such that it fits less perfectly to its analytical shape.

It has turned out that the very best solution to suppress the oscillation is computing the curvature by a smoothed phase-fraction field [99]. In our simulations, two smoothing iterations were sufficient.

## References

- [1] H. Kim, D. A. Boisen, J. M. Newhouse, B. L. Spatocco, B. Chung, P. J. Burke, D. J. Bradwell, K. Jiang, A. A. Tomaszowska, K. Wang, W. Wei, L. A. Ortiz, S. A.

- Barriga, S. M. Poizeau, D. R. Sadoway, Liquid Metal Batteries: Past, Present, and Future, *Chem. Rev.* 113 (3) (2013) 2075–2099. doi : 10.1021/cr300205k.
- [2] B. Agruss, H. R. Karas, V. L. Decker, Design and development of a liquid metal fuel cell, Tech. Rep. ASD-TDR-62-1045, General Motors Corporation (1962).
- [3] R. C. Vogel, M. Levenson, E. R. Proud, J. Royal, Chemical engineering division annual report - 1968, Tech. Rep. ANL-7575, Argonne National Laboratory (1969).
- [4] E. J. Cairns, R. K. Steunenber, High-temperature batteries, Tech. rep., Argonne National Laboratory (1973).
- [5] D. H. Kelley, T. Weier, Fluid mechanics of liquid metal batteries, *Appl. Mech. Rev.* 70 (2) (2018) 020801. doi : 10.1115/1.4038699.
- [6] B. Agruss, H. R. Karas, First Quarterly Technical Progress Report on Design and Development of a Liquid Metal Cell for the Period 1 January 1962 – 31 March 1962, Tech. Rep. AD 274 197, Armed Service Technical Information Agency (1962).
- [7] H. Shimotake, G. L. Rogers, E. J. Cairns, Secondary Cells with Lithium Anodes and Immobilized Fused-Salt Electrolytes, *Ind. Eng. Chem. Process Des. Dev.* 8 (1) (1969) 51–56.
- [8] R. C. Vogel, L. Burris, A. D. Tevebaugh, D. S. Webster, E. R. Proud, J. Royal, Chemical engineering division annual report - 1969, Tech. Rep. ANL-7675, Argonne National Laboratory (1970).
- [9] E. J. Cairns, H. Shimotake, High-Temperature Batteries, *Science* 164 (1969) 1347–1355.
- [10] R. D. Weaver, S. W. Smith, N. L. Willmann, The Sodium-Tin Liquid-Metal Cell, *J. Electrochem. Soc.* 109 (8) (1962) 653–657.

- [11] D. J. Bradwell, Liquid Metal Batteries: Ambipolar Electrolysis and Alkaline Earth Electroalloying Cells, Ph.D. thesis, Massachusetts Institute of Technology (2011).
- [12] J. Kim, Cell design/fabrication and optimization of cell components for rechargeable all-liquid metal batteries, Ph.D. thesis, Ulsan National Institute of Science and Technology (2017).
- [13] E. J. Cairns, E. Gay, V. Kolba, M. Kyle, A. D. Tevebaugh, L. Trevorow, Lithium/Selenium secondary cells for components in electric vehicular-propulsion generating systems, Tech. rep., Argonne National Laboratory (1970).
- [14] E. C. Gay, J. D. Arntzen, E. J. Cairns, J. E. Kincinas, J. G. Riha, L. E. Trevorow, W. J. Walsh, D. S. Webster, Lithium/chalcogen secondary cells for components in electric vehicular-propulsion generating systems, Tech. Rep. ANL-7863, Argonne National Laboratory (1972).
- [15] H. Kim, D. A. Boysen, T. Ouchi, D. R. Sadoway, Calcium - bismuth electrodes for large - scale energy storage (liquid metal batteries), *J. Power Sources* 241 (2013) 239–248.
- [16] J. Kim, D. Shin, Y. Jung, S. M. Hwang, T. Song, Y. Kim, U. Paik, LiCl-LiI molten salt electrolyte with bismuth-lead positive electrode for liquid metal battery, *J. Power Sources* 377 (2018) 87–92. doi : 10.1016/j.jpowsour.2017.11.081.
- [17] J.-S. Yeo, J.-H. Lee, E.-J. Yoo, Electrochemical properties of environment-friendly lithium-tin liquid metal battery, *Electrochim. Acta* 290 (2018) 228–235. doi : 10.1016/j.electacta.2018.09.072.
- [18] R. A. Beall, J. O. Borg, F. W. Wood, A study of consumable electrode arc melting, Tech. Rep. RI 5144, Bureau of Mines, USDI, Washington, D. C. (1955).
- [19] J. Campbell, Fluid flow and droplet formation in the electrosag remelting process, *JOM* 22 (7) (1970) 23–35.

- [20] Y. Shen, O. Zikanov, Thermal convection in a liquid metal battery, *Theor. Comput. Fluid Dyn.* 30 (4) (2016) 275–294. doi:10.1007/s00162-015-0378-1.
- [21] T. Köllner, T. Boeck, J. Schumacher, Thermal Rayleigh-Marangoni convection in a three-layer liquid-metal-battery model, *Phys. Rev. E* 95 (2017) 053114. doi:10.1103/PhysRevE.95.053114.
- [22] P. Personnettaz, P. Beckstein, S. Landgraf, T. Köllner, M. Nimtz, N. Weber, T. Weier, Thermally driven convection in Li||Bi liquid metal batteries, *J. Power Sources* 401 (2018) 362–374. doi:10.1016/j.jpowsour.2018.08.069.
- [23] F. Stefani, T. Weier, T. Gundrum, G. Gerbeth, How to circumvent the size limitation of liquid metal batteries due to the Tayler instability, *Energy Convers. Manag.* 52 (2011) 2982–2986. doi:10.1016/j.enconman.2011.03.003.
- [24] N. Weber, V. Galindo, F. Stefani, T. Weier, T. Wondrak, Numerical simulation of the Tayler instability in liquid metals, *New J. Phys.* 15 (2013) 043034. doi:10.1088/1367-2630/15/4/043034.
- [25] W. Herreman, C. Nore, L. Cappanera, J.-L. Guermond, Tayler instability in liquid metal columns and liquid metal batteries, *J. Fluid Mech.* 771 (2015) 79–114. doi:10.1017/jfm.2015.159.
- [26] N. Weber, V. Galindo, J. Priede, F. Stefani, T. Weier, The influence of current collectors on Tayler instability and electro vortex flows in liquid metal batteries, *Phys. Fluids* 27 (2015) 014103. doi:10.1063/1.4905325.
- [27] F. Stefani, V. Galindo, C. Kasprzyk, S. Landgraf, M. Seilmayer, M. Starace, N. Weber, T. Weier, Magnetohydrodynamic effects in liquid metal batteries, *IOP Conf. Ser. Mater. Sci. Eng.* 143 (2016) 012024. doi:10.1088/1757-899X/143/1/012024.
- [28] R. Ashour, D. H. Kelley, A. Salas, M. Starace, N. Weber, T. Weier, Competing forces in liquid metal electrodes and batteries, *J. Power Sources* 378 (2018) 301–310. doi:10.1016/j.jpowsour.2017.12.042.

- [29] W. Herreman, C. Nore, P. Z. Ramos, L. Cappanera, J.-L. Guermond, N. Weber, Numerical simulation of electro-vortex flows in cylindrical fluid layers and liquid metal batteries, *Phys. Rev. Fluids* 4 (2019) 113702.
- [30] K. Liu, F. Stefani, N. Weber, T. Weier, B. W. Li, Numerical and Experimental Investigation of Electro-Vortex Flow in a Cylindrical Container, *Magnetohydrodynamics* 56 (1) (2020) 27–41. doi:10.22364/mhd.56.1.3.
- [31] O. Zikanov, Metal pad instabilities in liquid metal batteries, *Phys. Rev. E* 92 (2015) 063021.
- [32] V. Bojarevics, A. Tucs, MHD of Large Scale Liquid Metal Batteries, in: A. P. Ratvik (Ed.), *Light Metals 2017*, Springer International Publishing, Cham, 2017, pp. 687–692.
- [33] N. Weber, P. Beckstein, W. Herreman, G. M. Horstmann, C. Nore, F. Stefani, T. Weier, Sloshing instability and electrolyte layer rupture in liquid metal batteries, *Phys. Fluids* 29 (5) (2017) 054101. doi:10.1063/1.4982900.
- [34] O. Zikanov, Shallow water modeling of rolling pad instability in liquid metal batteries, *Theor. Comput. Fluid Dyn.* 32 (3) (2018) 325–347.
- [35] G. M. Horstmann, N. Weber, T. Weier, Coupling and stability of interfacial waves in liquid metal batteries, *J. Fluid Mech.* 845 (2018) 1–35. doi:10.1017/jfm.2018.223.
- [36] S. Molokov, The nature of interfacial instabilities in liquid metal batteries in a vertical magnetic field, *EPL Europhys. Lett.* 121 (4) (2018) 44001. doi:10.1209/0295-5075/121/44001.
- [37] A. Tucs, V. Bojarevics, K. Pericleous, MHD stability of large scale liquid metal batteries, *J. Fluid Mech.* 852 (2018) 453–483.
- [38] A. Tucs, V. Bojarevics, K. Pericleous, Magneto-hydrodynamic stability of a liquid metal battery in discharge, *EPL* 124 (2) (2018) 24001. doi:10.1209/0295-5075/124/24001.

- [39] W. Herreman, C. Nore, J.-L. Guermond, L. Cappanera, N. Weber, G. M. Horstmann, Perturbation theory for metal pad roll instability in cylindrical reduction cells, *J. Fluid Mech.* 878 (2019) 598–646. doi:10.1017/jfm.2019.642.
- [40] L. Xiang, O. Zikanov, Numerical simulation of rolling pad instability in cuboid liquid metal batteries, *Phys. Fluids* 31 (12) (2019) 124104. doi:10.1063/1.5123170.
- [41] G. M. Horstmann, M. Wylega, T. Weier, Measurement of interfacial wave dynamics in orbitally shaken cylindrical containers using ultrasound pulse-echo techniques, *Exp. Fluids* 60 (4) (2019). doi:10.1007/s00348-019-2699-0.
- [42] G. M. Horstmann, W. Herreman, T. Weier, Linear damped interfacial wave theory for an orbitally shaken upright circular cylinder, *J. Fluid Mech.* 891 (2020) A22. doi:10.1017/jfm.2020.163.
- [43] A. D. Sneddy, Stability of fluid layers carrying a normal electric current, *J. Fluid Mech.* 156 (1985) 223–236.
- [44] J. Priede, Stability of fluid layers carrying a normal electric current revisited, Tech. rep., Coventry University (2016).
- [45] U. Ingard, D. S. Wiley, Instabilities of a liquid conductor, *Phys. Fluids* 5 (12) (1962) 1500.
- [46] J. Newman, K. E. Thomas-Alyea, *Electrochemical Systems*, John Wiley & Sons, 2004.
- [47] C. Christiansen, Kapillarelektische Bewegungen, *Ann. Phys.* 317 (13) (1903) 1072–1079. doi:10.1002/andp.19033171309.
- [48] A. Frumkin, B. Levich, The Motion of Solid and Liquid Metallic Bodies in Solutions of Electrolytes, *Acta Physicochim. URSS* 20 (1945).
- [49] C. J. Allum, Metal transfer in arc welding as a varicose instability. I. Varicose instabilities in a current-carrying liquid cylinder with surface charge, *J. Phys. D: Appl. Phys.* 18 (7) (1985) 1431–1446. doi:10.1088/0022-3727/18/7/029.

- [50] S. Rhee, E. Kannatey-Asibu, Observation of metal transfer during gas metal arc welding, *Weld. J.* 115 (1992) 381–386.
- [51] V. A. Nemchinsky, The effect of the type of plasma gas on current constriction at the molten tip of an arc electrode, *J. Phys. D: Appl. Phys.* 29 (5) (1996) 1202–1208. doi:10.1088/0022-3727/29/5/014.
- [52] W. J. Greene, An analysis of transfer in gas-shielded welding arcs, *Trans. Am. Inst. Electr. Eng. Part II Appl. Ind.* 79 (3) (1960) 194–203.
- [53] J. C. Amson, Lorentz force in the molten tip of an arc electrode, *Br. J. Appl. Phys.* 16 (8) (1965) 1169.
- [54] Y.-S. Kim, T. W. Eagar, Analysis of Metal Transfer in Gas Metal Arc Welding, *Weld. J.* 72 (6) (1993) 269–278.
- [55] C. Hering, A practical limitation of resistance furnaces; the "pinch" phenomenon, *Transactions of the American Electrochemical Society* 11 (1907) 329–337.
- [56] E. F. Northrup, Some newly observed manifestations of forces in the interior of an electric conductor, *Phys. Rev. Ser. I* 24 (6) (1907) 474.
- [57] R. A. Alpher, Experiments in magneto-fluid dynamics, *Phys. Today* 13 (12) (1960) 26–31.
- [58] A. Kharicha, M. Wu, A. Ludwig, M. Ramprecht, H. Holzgruber, Influence of the frequency of the applied ac current on the electrosag remelting process, in: *CFD Modeling and Simulation in Materials Processing, CFD Modeling and Simulation in Materials Processing*, John Wiley & Sons, Inc., 2012, Ch. 17, pp. 139–146.
- [59] F. J. Zanner, Metal transfer during vacuum consumable arc remelting, *Metall. Trans. B* 10 (2) (1979) 133–142.
- [60] A. Kharicha, M. Wu, A. Ludwig, E. Karimi-Sibaki, Simulation of the Electric Signal During the Formation and Departure of Droplets in the Electrosag Remelting Process, *Metall. Mater. Trans. B* 47 (2) (2016) 1427–1434. doi:10.1007/s11663-015-0550-4.

- [61] B. Korousic, Tropfenbildung beim Elektro-Schlacke-Umschmelzverfahren, *Archiv für das Eisenhüttenwesen* 47 (1976) 283–288.
- [62] A. Kharicha, M. Wu, A. Ludwig, E. Karimi-Sibaki, Simulation of the electric signal during the formation and departure of droplets in the electroslag remelting process, *Metallurgical and Materials Transactions B* 47 (2) (2016) 1427–1434.
- [63] X. Ning, S. Phadke, B. Chung, H. Yin, P. Burke, D. R. Sadoway, Self-healing Li–Bi liquid metal battery for grid-scale energy storage, *J. Power Sources* 275 (2015) 370–376. doi:10.1016/j.jpowsour.2014.10.173.
- [64] S. J. Zinkle, Summary of Physical Properties for Lithium, Pb-17Li, and (LiF)<sub>n</sub>•BeF<sub>2</sub> Coolants, in: APEX Study Meeting, Sandia National Laboratories, 1998.
- [65] G. J. Janz, R. P. T. Tomkins, C. B. Allen, Molten Salts: Volume 4, Part 4 Mixed Halide Melts Electrical Conductance, Density, Viscosity, and Surface Tension Data, *J. Phys. Chem. Ref. Data* 8 (1) (1979) 125. doi:10.1063/1.555590.
- [66] V. Sobolev, Database of Thermophysical Properties of Liquid Metal Coolants for GEN-IV, SCK CEN, 2010.
- [67] B. B. Alchagirov, F. F. Dyshekova, R. K. Arkhestov, O. K. Kyasova, Surface tension and adsorption of lithium in bismuth-based alloys, *Bull. Russ. Acad. Sci. Phys.* 80 (11) (2016) 1381–1384. doi:10.3103/S1062873816110071.
- [68] H. Rusche, Computational Fluid Dynamics of Dispersed Two-Phase Flows at High Phase Fractions, Ph.D. thesis, Imperial College London (2002).
- [69] J. U. Brackbill, D. B. Kothe, C. Zemach, A continuum method for modeling surface tension, *J. Comput. Phys.* 100 (1992) 335–354.
- [70] K. W. Lam, A Numerical Surface tension Model for Two-Phase Flow Simulations, Ph.D. thesis, University of Groningen, Groningen (2009).

- [71] W. Wang, K. Wang, Simulation of thermal properties of the liquid metal batteries, in: 6th International Conference on Power Electronics Systems and Applications (PESA), IEEE, 2015, pp. 1–11.
- [72] K. Kissling, J. Springer, H. Jasak, S. Schutz, K. Urban, M. Piesche, A coupled pressure based solution algorithm based on the volume-of-fluid approach for two or more immiscible fluids, in: V European Conference on Computational Fluid Dynamics, ECCOMAS CFD, 2010.
- [73] N. Weber, V. Galindo, F. Stefani, T. Weier, The Tayler instability at low magnetic Prandtl numbers: Between chiral symmetry breaking and helicity oscillations, *New J. Phys.* 17 (11) (2015) 113013. doi:10.1088/1367-2630/17/11/113013.
- [74] V. Bandaru, T. Boeck, D. Krasnov, J. Schumacher, A hybrid finite difference–boundary element procedure for the simulation of turbulent MHD duct flow at finite magnetic Reynolds number, *J. Comput. Phys.* 304 (2016) 320–339.
- [75] C. Hirt, B. Nichols, Volume of fluid (VOF) method for the dynamics of free boundaries, *J. Comput. Phys.* 39 (1) (1981) 201–225. doi:10.1016/0021-9991(81)90145-5.
- [76] O. Ubbink, Numerical prediction of two fluid systems with sharp interfaces, Ph.D. thesis, University of London (1997).
- [77] M. Graveleau, Pore-Scale Simulation of Mass Transfer Across Immiscible Interfaces, Tech. rep., Stanford University (2016).
- [78] J. P. Boris, D. L. Book, Flux-corrected transport. I. SHASTA, a fluid transport algorithm that works, *J. Comput. Phys.* 11 (1) (1973) 38–69. doi:10.1016/0021-9991(73)90147-2.
- [79] S. Zalesak, Fully Multidimensional Flux-Corrected Algorithms for Fluids, *J. Comput. Phys.* 31 (1979) 335–362.

- [80] S. M. Damián, An Extended Mixture Model for the Simultaneous Treatment of Short and Long Scale Interfaces, Ph.D. thesis, Universidad Nacional del Litoral, Santa Fe, Argentina (2013).
- [81] M. Rudman, Volume-tracking methods for interfacial flow calculations, *Int. J. Numer. Methods Fluids* 24 (7) (1997) 671–691. doi:10.1002/(SICI)1097-0363(19970415)24:7<671::AID-FLD508>3.0.CO;2-9.
- [82] H. G. Weller, G. Tabor, H. Jasak, C. Fureby, A tensorial approach to computational continuum mechanics using object-oriented techniques, *Comput. Phys.* 12 (6) (1998) 620–631.
- [83] A. J. Meir, P. G. Schmidt, A velocity-current formulation for stationary MHD flow, *Appl. Math. Comput.* 65 (1994) 95–109.
- [84] N. Weber, P. Beckstein, V. Galindo, M. Starace, T. Weier, Electro-vortex flow simulation using coupled meshes, *Comput. Fluids* 168 (2018) 101–109. doi:10.1016/j.compfluid.2018.03.047.
- [85] P. Fiflis, A. Press, W. Xu, D. Andruczyk, D. Curreli, D. Ruzic, Wetting properties of liquid lithium on select fusion relevant surfaces, *Fusion Eng. Des.* 89 (12) (2014) 2827 – 2832. doi:10.1016/j.fusengdes.2014.03.060.
- [86] G. Z. Zuo, J. S. Hu, J. Ren, Z. Sun, Q. X. Yang, J. G. Li, L. E. Zakharov, D. K. Mansfield, Methods and preliminary measurement results of liquid Li wettability, *Rev. Sci. Instrum.* 85 (2) (2014) 023506. doi:10.1063/1.4865118.
- [87] S. Krat, A. Popkov, Y. M. Gasparyan, A. Pisarev, P. Fiflis, M. Szott, M. Christenson, K. Kalathiparambil, D. N. Ruzic, Wetting properties of liquid lithium on lithium compounds, *Fusion Eng. Des.* 117 (2017) 199 – 203. doi:10.1016/j.fusengdes.2016.06.038.
- [88] A. Cassie, S. Baxter, Wettability of porous surfaces, *Transactions of the Faraday society* 40 (1944) 546–551.

- [89] J. T. Korhonen, Young-laplace equation solver for axisymmetric drop-shape analysis (ADSA), <https://version.aalto.fi/gitlab/jtkorho2/drop-solver> (2018).
- [90] E. J. Cairns, C. E. Crouthamel, A. K. Fischer, M. S. Foster, J. C. Hesson, C. E. Johnson, H. Shimotake, A. D. Tevebaugh, Galvanic Cells with Fused-Salt Electrolytes, ANL-7316, Argonne National Laboratory, 1967.
- [91] T. Weier, I. Grants, G. Horstmann, S. Landgraf, M. Nimtz, P. Personnetaz, F. Stefani, N. Weber, Conductivity influence on interfacial waves in liquid metal batteries and related two-layer systems, *Magneto hydrodynamics* 56 (2020) 237–245.
- [92] M. Guilizzoni, Drop shape visualization and contact angle measurement on curved surfaces, *J. Colloid Interface Sci.* 364 (1) (2011) 230–236. doi:10.1016/j.jcis.2011.08.019.
- [93] M. Guilizzoni, Drop deposition and low-speed impact on flat, curved and microfinned solid surfaces: comparison between simulations, models and experiments, in: *DIPSI Workshop 2012 on Droplet Impact Phenomena & Spray Investigation*, 2012, pp. 23–32.
- [94] C. Kunkelmann, Numerical Modeling and Investigation of Boiling Phenomena, Ph.D. thesis, Technische Universität Darmstadt (2011).
- [95] T. Maurer, Experimentelle und numerische Untersuchung der Tropfenbewegung unter Einfluss von äußeren Kräften, Ph.D. thesis, Bergische Universität Wuppertal (2016).
- [96] P. Horgue, M. Prat, M. Quintard, A penalization technique applied to the “Volume-Of-Fluid” method: Wettability condition on immersed boundaries, *Comput. Fluids* 100 (2014) 255–266. doi:10.1016/j.compfluid.2014.05.027.
- [97] M. J. Nieves-Remacha, L. Yang, K. F. Jensen, OpenFOAM Computational Fluid Dynamic Simulations of Two-Phase Flow and Mass Transfer in an Advanced-Flow Reactor, *Ind. Eng. Chem. Res.* 54 (26) (2015) 6649–6659. doi:10.1021/acs.iecr.5b00480.

- [98] T. Naoe, M. Futakawa, R. G. Kenny, M. Otsuki, Experimental and numerical investigations of liquid mercury droplet impacts, *J. Fluid Sci. Technol.* 9 (1) (2014) 13–00248. doi:10.1299/jfst.2014jfst0002.
- [99] D. A. Hoang, V. van Steijn, L. M. Portela, M. T. Kreutzer, C. R. Kleijn, Benchmark numerical simulations of segmented two-phase flows in microchannels using the Volume of Fluid method, *Comput. Fluids* 86 (2013) 28–36.